

## Article

# Analytical Method for Designing Three-Phase Air-Gapped Compensation Choke

Vladimir Kindl <sup>1</sup>, Lukáš Sobotka <sup>1</sup>, Michal Frivaldsky <sup>2,\*</sup> and Martin Skalicky <sup>1</sup>

<sup>1</sup> Research and Innovation Centre for Electrical Engineering (RICE), Faculty of Electrical Engineering, University of West Bohemia, Univerzitní 8, 306 14 Pilsen, Czech Republic

<sup>2</sup> Department of Electronics and Mechatronics, Faculty of Electrical Engineering and Information Technologies, University of Zilina, Zilina 010 26, Slovakia

\* Correspondence: michal.frivaldsky@feit.uniza.sk

**Abstract:** The compensating choke plays an important role in many high-power industrial applications with reactive power compensation. Due to the high number of devices installed every year and the EU's efforts to reduce the energy demands of our society, it is advisable to maximize the efficiency of these devices. Due to the non-linearity of the magnetic core, the requirement of a linear operating characteristic, and the presence of a distributed air gap, this is a difficult task, with various technical challenges. This paper presents an analytical method for the electromagnetic design of a three-phase compensating choke with an air-gapped core and a flat load characteristic. The design method considers the fringing magnetic fields and the current-density dimensioning based on an advanced analytical thermal model. The proposed method is based on the use of existing analytical procedures; however, optimization was conducted to achieve a trade-off between the core and the  $I^2R$  losses to manipulate the efficiency and the weight and identify optimization possibilities. The presented method was verified by the finite element method (FEM) using the engineering-simulation software, ANSYS.



**Citation:** Kindl, V.; Sobotka, L.; Frivaldsky, M.; Skalicky, M.

Analytical Method for Designing Three-Phase Air-Gapped Compensation Choke. *Energies* **2022**, *15*, 7328. <https://doi.org/10.3390/en15197328>

Academic Editor: K.T. Chau

Received: 29 July 2022

Accepted: 29 September 2022

Published: 5 October 2022

**Publisher's Note:** MDPI stays neutral with regard to jurisdictional claims in published maps and institutional affiliations.



**Copyright:** © 2022 by the authors. Licensee MDPI, Basel, Switzerland. This article is an open access article distributed under the terms and conditions of the Creative Commons Attribution (CC BY) license (<https://creativecommons.org/licenses/by/4.0/>).

**Keywords:** compensation; choke; analytical; design; optimization

## 1. Introduction

The compensating choke plays an important role in many high-power industrial applications with reactive power compensation, e.g., metal-clad HV cables, long distribution and transmission grids, photovoltaic power plants, etc.

High linearity is needed from the compensation choke, i.e., constant inductance up to the defined working current and low losses, as the choke works continuously. These features are mostly intended for one operating frequency and are made from high-quality transformer sheets with a copper or aluminum flat-wire winding; smaller types are wound with a round copper wire. Vacuum impregnation with a special resin ensures high resistance to voltage stress, minimal noise (no resonance), and long service life. In addition, the chokes are usually equipped with a thermal bimetallic sensor to prevent overheating and must meet the requirements of the EN 60289:1994 and EN 61558-2-20:2011 standards.

Chokes are common parts used in industry, and millions of new units are installed each year. Even a slight increase in the efficiency of these new components will, therefore, significantly contribute to the global reduction in electricity consumption and thus support the commitments of the EU, which has adopted very ambitious targets to reduce net greenhouse-gas emissions by a further 55% by 2030 compared to 1990 levels [1–3]. Efficiency optimization is not an easy task considering electromagnetic use as a determining parameter, since it affects not only the losses but also the volume and, thus, the weight and, consequently, the power density of the resulting design. This situation becomes even more complicated when designing the air-gapped choke, which must provide stable self-inductance up to the rated or, in this case, maximum current.

Inductive components and their design and analysis have been widely investigated during the development of various power and industrial systems. The literature covers numerous design methods, including loss analysis and energy efficiency [4–12]. Reference [8] reports a detailed analytical method for the electromagnetic design of four possible architectures—UI-, EI-, Y-, and delta-core. Although the study was partly concerned with efficiency optimization, and the authors showed that Y-core and delta-core inductors can reduce mass for a given loss, it does not consider the best ratio of iron-core and  $I^2R$  losses for maximum efficiency. Another interesting approach to this issue was proposed in [9], where the authors presented a comprehensive physical characterization and modeling of the three-phase common-mode inductors, along with the equivalent circuits that were relevant to their design. However, this study is not readily applicable to three-phase air-gapped inductors. The authors of [10] developed a novel design and optimization method for power inductors for three-phase high-power-density inverters suitable for aircraft applications. The study considered the inductor's geometric parameters, magnetic properties, core-material selection, core, and copper losses, in addition to temperature calculations to determine the low-losses design, and used a multi-goal optimization algorithm to calculate the weight, volume, and current ripples for different switching frequencies and different inductor core materials. A key limitation of this research is that it did not consider the flat operating characteristic typical of compensating chokes and, therefore, did not include or mention the calculation of the optimal air gap. Another interesting report is [11]. The authors proposed analytical equations to estimate the magnetic flux density, including the fringing magnetic flux, and derived the formulas to find the size of a single or multiple air gaps. However, their approach dealt with high-frequency chokes, which have slightly different requirements from compensation chokes and use different materials and core shapes. This also applies to the work presented in [12,13], which, although thematically close, propose an advanced analytical model for calculating the winding losses in gapped magnetic components using a ferrite magnetic core with linear permeability. These methods are based on a simplified magnetic-field calculation and are suitable for the low–medium–frequency range.

Therefore, these studies do not suit the electromagnetic design of the compensation choke. Several other works related to the topic are worth mentioning, e.g., [14–23]; however, their application is also dedicated to power electronics rather than energetics. As far as we know, studies on this topic have still not been completed. Therefore, we developed and proposed our design method for compensation chokes.

This paper presents a procedure for the first electromagnetic design of a three-phase compensating choke with a flat load characteristic, including the advanced analytical sizing of the current density concerning specific temperature conditions. As an input, the procedure requires the setting of the electromagnetic use values, the maximum (or saturation) current, and the desired nominal inductance. It allows the targeted variation of the ratio between the losses produced in the core and in the windings, thus choosing the best design in terms of losses or weight. The proposed method is based on a single-phase choke design, and the resulting formulas are therefore simpler and easier to implement, even in an Excel sheet, which is potentially interesting for electrical engineers. The method includes a detailed calculation of fringing magnetic fields necessary for correct air-gap setting and considers very precisely the thermal conditions, which significantly shortens the entire design process and thus reduces the overall costs. The efficacy of the method is proven in a case study and verified by finite-element analyses using the engineering-simulation software, ANSYS.

## 2. Design Equation

The inductance of the single-phase choke is generally given by Equation (1),

$$L = \frac{N^2}{R_m} = \mu_0 \mu_{eff} \frac{N^2}{l_c} S_{fe} \quad (1)$$

where  $\mu_{eff}$  is the effective permeability of the core,  $l_c$  is the average length of flux line,  $N$  is the number of turns, and  $S_{fe}$  denotes the cross-section area of the magnetic core. Ampere's law shows the maximum value of the magnetic field strength (2),

$$H_{max} = \frac{I_{1mag}N}{l_c} \quad (2)$$

where the  $H_{max}$  is maximum of the magnetic-field strength and  $I_{1mag}$  is the size of the current. To make the design process more general, we represent the current by its rms value using the form factor  $K_f$  given in (3).

$$I_1 = I_{1mag}K_f \quad (3)$$

$$K_f = \frac{1}{\sqrt{\frac{1}{T} \int_0^T \left( \frac{i_1(t)}{I_{1mag}} \right)^2 dt}} \quad (4)$$

In (3)  $i_1(t)$  is the choke current and  $T$  is the time of one period. Further, we change (2) into (5), which brings  $B_{max}$  into the equation as an important sizing parameter in the design process.

$$I_{1mag} = \frac{B_{max}l_c}{\mu_0\mu_{eff}N} \quad (5)$$

This value directly affects the core use and, hence, the weight and cost of the choke's magnetic core.

### 2.1. $I^2R$ Losses

The  $I^2R$  losses  $I_1^2R$  are calculated based on the mean length of the coil turn  $l_{Zavg}$  and from the cross-section area of the conductor  $S_Z$  using (6).

$$P_{cu} = \rho_{cu} \frac{l_w}{S_Z} I_1^2 = \rho_{cu} \frac{l_{Zavg}N}{S_Z} \left( I_{1mag}K_f \right)^2 \quad (6)$$

In (6),  $P_{cu}$  represents  $I^2R$  losses,  $l_w$  is the net length of the coil wire, and  $\rho_{cu}$  is the material's electrical resistivity.

The resulting magnitude of the current is then as in (7).

$$I_{1mag} = \frac{1}{K_f N} \sqrt{\frac{P_{cu} N S_Z}{\rho_{cu} l_{Zavg}}} \quad (7)$$

### 2.2. Effective Permeability Optimization

In principle, the choke acts as the magnetic-energy storage; therefore, we proceed from the assumption of its maximum value (8).

$$\frac{1}{2} L I_{1mag}^2 = \frac{1}{2} \frac{l_c S_{fe}}{\mu_0 \mu_{eff}} B_{max}^2 \quad (8)$$

Considering  $I^2R$  losses, (8) changes into (9).

$$\frac{1}{2} L I_{1mag}^2 = \frac{1}{2} \frac{\mu_0 \mu_{eff} S_{fe} S_Z N}{\rho_{cu} l_{Zavg} l_c K_f^2} P_{cu} \quad (9)$$

Both Equations (8) and (9) express the magnetic energy stored by the choke as dependent on the effective permeability  $\mu_{eff}$ , maximum winding losses  $P_{cu}$  (or  $I^2R$ ), and maximum core saturation  $B_{max}$ . From this, we can construct the design region (shown in Figure 1), restricted on each side by the maximum permitted  $I^2R$  losses (left side), the core saturation

(right side), and the stored energy (from above). The curves for  $LI_{1mag}^2$ , calculated by (8) and (9), are drawn for three values of  $\mu_{eff}$ .

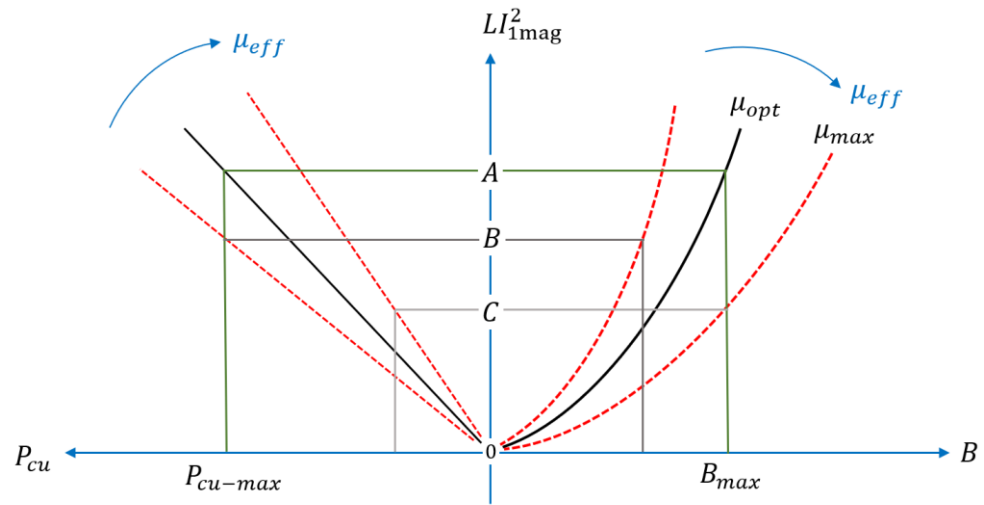


Figure 1. Optimal effective permeability.

The solid lines (point “A”) show the energy stored for the best  $\mu_{eff} = \mu_{opt}$ , which is also the maximum for the core. In this case, the choke accumulates the highest possible magnetic energy, while both the core and the winding are fully electromagnetically utilized, i.e., the highest core saturation and  $I^2R$  losses are achieved. At design point “B”, the choke generates maximum  $I^2R$  losses, but is slightly less saturated, which results in lower stored energy. Hence,  $\mu_{eff} < \mu_{opt}$ . The point “C” corresponds to a situation with a fully saturated magnetic core, but lowered  $I^2R$  losses and stored magnetic energy, i.e.,  $\mu_{eff} > \mu_{opt}$ .

Comparing (5) and (7), we obtain the optimal effective permeability (10),

$$\frac{B_{max}l_c}{\mu_0\mu_{eff}N} = \frac{1}{K_f N} \sqrt{\frac{P_{cu-max}NSZ}{\rho_{cu}l_{Zavg}}} \Rightarrow \mu_{opt} = \frac{B_{max}l_c K_f}{\mu_0 \sqrt{\frac{P_{cu-max}NSZ}{\rho_{cu}l_{Zavg}}}} \tag{10}$$

which can be further refined by implementing the slot-filling factor  $k_u$ , as in (11). The slot-filling factor is the ratio of the net conductive cross-sectional area of all the winding conductors  $S_{cu}$  to the winding-window cross-section area  $S_w$ .

$$k_u = \frac{S_{cu}}{S_w} = \frac{NSZ}{S_w} \tag{11}$$

The optimal permeability is then calculated by (12).

$$\mu_{opt} = \frac{B_{max}l_c K_f}{\mu_0 \sqrt{\frac{P_{cu-max}k_u S_w}{\rho_{cu}l_{Zavg}}}} \tag{12}$$

The choke is well designed when  $\mu_{eff} \approx \mu_{opt}$ . The magnetic-core reluctance is formed by a series connection of two components (13), the reluctance of the iron core, and the reluctance of the air gap.

$$R_{m-eq} = R_{m-fe} + R_{m-\delta} = \frac{l_c - \delta}{\mu_r \mu_0 S_{fe}} + \frac{\delta}{\mu_0 S_{\delta}} \tag{13}$$

In most real cases, the air-gap size is negligible compared to the core dimensions. Therefore, we can simplify (13) by assuming that  $S_{fe} = S_{\delta}$  resulting in (14).

$$R_{m-eq} \approx \frac{l_c - \delta}{\mu_r \mu_0 S_{fe}} + \frac{\delta}{\mu_0 S_{fe}} \approx \frac{l_c}{\mu_0 S_{fe}} \left[ \frac{1 - \frac{\delta}{l_c}}{\mu_r} + \frac{\delta}{l_c} \right] \tag{14}$$

The ratio  $\delta/l_c$  located in the first fraction within the brackets gives very a low value ( $\delta/l_c \approx 0$ ). Thus, (14) can be simplified into (15).

$$R_{m-eq} \approx \frac{l_c}{\mu_0 S_{fe}} \left[ \frac{1}{\mu_r} + \frac{1}{l_c/\delta} \right] = \frac{l_c}{\mu_{eff} \mu_0 S_{fe}} \tag{15}$$

The effective permeability is then (16), derived from (15).

$$\mu_{eff} = \frac{1}{\frac{1}{\mu_r} + \frac{1}{l_c/\delta}} \tag{16}$$

### 2.3. Fringing Magnetic Flux

It is not an easy task to describe the effect of the fringing magnetic flux by an analytical method. A good analysis is proposed in [14], but the presented results do not apply well to this task.

The leakage flux in the air gap is illustrated in Figure 2. Considering this, we can write (17), where  $L'$  is the inductance increase due to the leakage of magnetic flux.

$$L' = \frac{N^2}{R_{fe} + R'_{\delta}} \approx \frac{N^2}{R'_{\delta}} = L \frac{S_{\delta}}{S_{fe}} = L \frac{(a + \delta)^2}{a^2} = L \frac{a^2 + 2a\delta + \delta^2}{a^2} \tag{17}$$

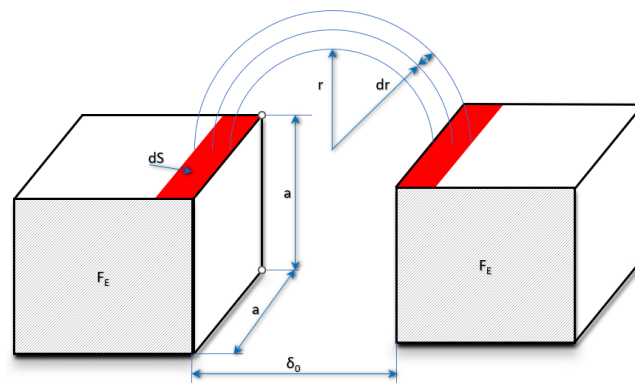
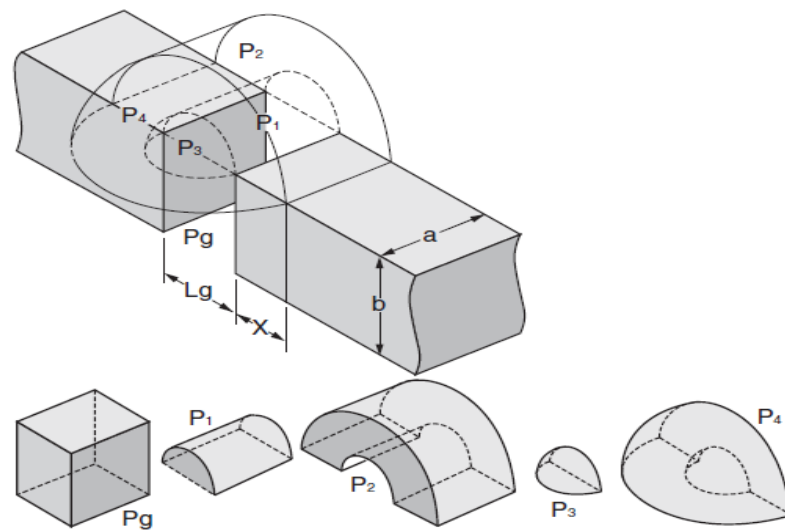


Figure 2. Simplified magnetic leakage field.

Assuming  $\delta^2/a^2 \approx 0$ , we obtain (18).

$$L' \approx L \left( 1 + 2 \frac{\delta}{a} \right) \tag{18}$$

Although the calculation of (18) is fast, its result is only approximate. A more accurate approach is indicated in Figure 3.



**Figure 3.** Geometric elements used for the description of the magnetic leakage flux [15].

In this case, the approximating element  $P_g$  considers an homogenous magnetic field with parallel flux lines. In  $P_1$  and  $P_3$ , the flux lines arise from a geometry with a zero-cross-section area, which does not correspond well to the actual situation. However, it is possible to improve this by considering all the elements,  $P_1$ ,  $P_3$ , and  $P_g$  as a single region (see Figure 4). The analysis is calculated further with magnetic reluctances, which can easily be converted to inductances.

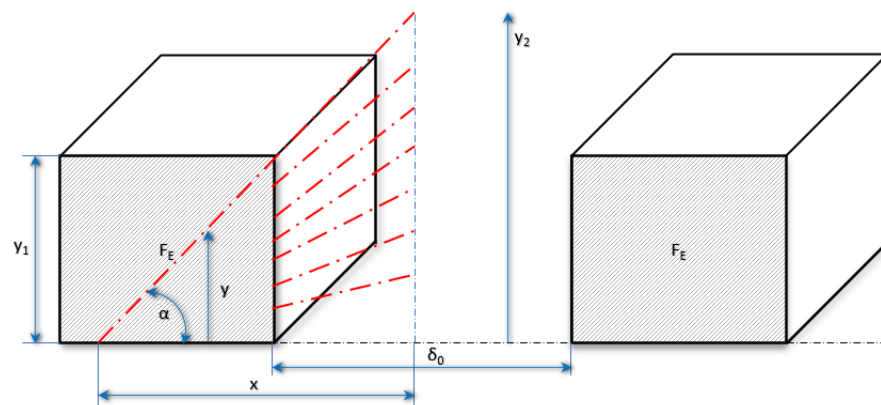


**Figure 4.** The illustration of the geometry of the elements  $P_g$ ,  $P_1$ , and  $P_3$ .

The reluctance element for the magnetic flux shown in Figure 4 is given by (19),

$$dR_{m-h} = \frac{dx}{\mu_0 4y^2} \tag{19}$$

where (20) defines the relationship between  $dx$  and  $dy$ .

$$dx = \frac{\delta_0}{2(y_2 - y_1)} dy \tag{20}$$

Substituting (20) back into (19), formula (21) is obtained.

$$R_{m-h} = \frac{2}{\mu_0 4} \int_{y_1}^{y_2} \frac{\delta_0}{2(y_2 - y_1)y^2} dy = \frac{\delta_0}{\mu_0 4y_1 y_2} \tag{21}$$

Considering the integration limits, i.e.,  $y_1 = \frac{a}{2}$ ,  $y_2 = \frac{(a+\delta_0)}{2}$ , we find the reluctance as (22).

$$R_{m-h} = \frac{\delta_0}{\mu_0 a (a + \delta_0)} \tag{22}$$

The element  $P_2$  is partly described in the previous section, in Figure 2, and the reluctance of this element is (23).

$$R_{m-2} = \frac{1}{\mu_0 \frac{2a}{\pi} \ln\left(\frac{r_2}{r_1}\right)} \tag{23}$$

Assuming the geometrical situation shown in Figure 4, we can determine the reluctance of the last element,  $P_4$ . The analysis is based on the idea of a drilled hollow ball (Figure 5). We start with (24).

$$dR_{m-3} = \frac{dl}{\mu_0 S_k} \tag{24}$$

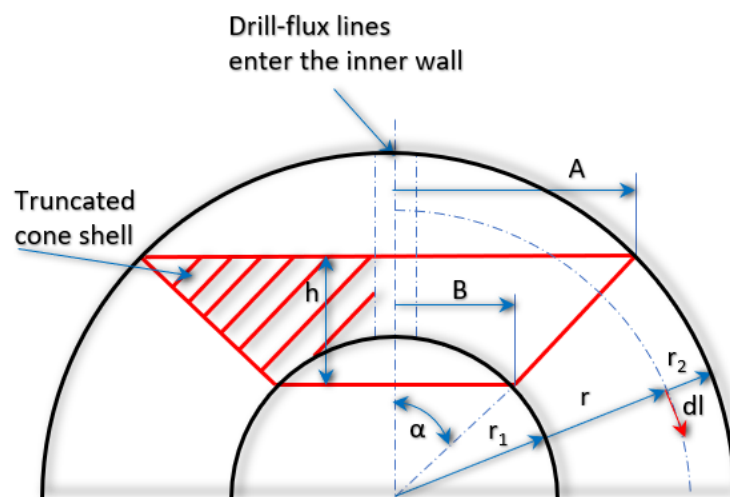


Figure 5. Illustrative geometry to derive reluctance of the element  $P_4$ .

The correct procedure would be to integrate over the radius  $r$  and the angle  $\alpha$ ; however, since the length of the flux line equals its mean value, we use this fact to simplify the task. The cross-sectional area, through which the flux lines pass, has the shape of a truncated cone shell and is given by Equation (25).

$$S_k = \pi(A + B)\sqrt{h^2 + (A - B)^2} \tag{25}$$

Substituting into (25) we obtain (26).

$$S_k = \pi(r_1 + r_2)\sin\alpha\sqrt{[(r_2 - r_1)\cos\alpha]^2 + [(r_2 - r_1)\sin\alpha]^2} = \pi(r_2^2 - r_1^2)\sin\alpha \tag{26}$$

The actual investigated region has only a quarter area. Thus, we integrate only the first  $90^\circ$ , resulting in (27),

$$R_{m-3} = \frac{2r_1+r_2}{\mu_0 4\pi (r_2^2 - r_1^2)} \int_0^{\pi/2} \frac{d\alpha}{\sin\alpha} = \frac{r_1 + r_2}{\mu_0 4\pi (r_2^2 - r_1^2)} \int_0^{\pi/2} \csc\alpha d\alpha \tag{27}$$

where (28) is an indefinite integral.

$$\int \csc\alpha d\alpha = -\ln|\csc\alpha + \cot\alpha| + c \tag{28}$$

After considering the integration limits, (28) gives (29).

$$R_{m-3} = \frac{r_1 + r_2}{\mu_0 4\pi (r_2^2 - r_1^2)} \ln |\csc 0 + \cot 0| \quad (29)$$

Examining (29), we find that it is a divergent integral, which is fully consistent with the selected geometry of the approximation element  $P_4$ , in which the flux lines arise from the zero-cross-section area. The only way to solve this problem is to start the integration from values slightly higher than 0.

#### 2.4. The Optimization of the Losses

We start with the power Equation (30),

$$S_1 = K_v k_{stack} k_u f B_{max} J_1 S_w S_{fe} \quad (30)$$

where  $K_v$  is the voltage-form factor and  $k_{stack}$  is the core-lamination-filling factor. Equation (30) is simplified by merging the cross-section area of the core and the winding, so that  $S_{w-fe} = S_w S_{fe}$ .

$$S_1 = K_v k_{stack} k_u f B_{max} J_1 S_{w-fe} \quad (31)$$

From (31), we obtain the current density (32):

$$J_1 = \frac{S_1}{K_v k_{stack} k_u f B_{max} S_{w-fe}} \quad (32)$$

The  $I^2R$ -losses formula is adjusted to (33) and, combined with (32), it gives (34).

$$P_{cu} = R_1 I_1^2 = \rho_{cu} \frac{l_{Zavg} N}{S_Z} (S_Z J_1)^2 = \rho_{cu} l_{Zavg} N S_Z J_1^2 = \rho_{cu} k_u S_w l_{Zavg} J_1^2 \quad (33)$$

$$P_{cu} = \rho_{cu} k_u S_w l_{Zavg} \left( \frac{S_1}{K_v k_{stack} k_u f B_{max} J_1 S_{w-fe}} \right)^2 = \frac{\rho_{cu} S_w l_{Zavg} S_1^2}{K_v^2 k_{stack}^2 k_u f^2 B_{max}^2 S_{w-fe}^2} \quad (34)$$

Introducing the substitution of (35), we obtain (36).

$$a_1 = \frac{\rho_{cu} S_w l_{Zavg} S_1^2}{K_v^2 k_{stack}^2 k_u S_{w-fe}^2} \quad (35)$$

$$P_{cu} = \frac{a_1}{f^2 B_{max}^2} \quad (36)$$

The iron-core losses (37) are usually calculated based on Steinmetz's coefficient  $K_c$ , exponents  $\alpha$  and  $\beta$ , and the iron-core volume  $V_{fe}$ .

$$P_{fe} = K_c V_{fe} f^\alpha B_{max}^\beta \quad (37)$$

Substituting (38) back into (37) we obtain (39).

$$b_1 = K_c V_{fe} \quad (38)$$

$$P_{fe} = b_1 f^\alpha B_{max}^\beta \quad (39)$$

The total losses (40) are further obtained by the summation of (36) and (39).

$$P_{net} = \frac{a_1}{f^2 B_{max}^2} + b_1 f^\alpha B_{max}^\beta \quad (40)$$

#### 2.4.1. Constant Frequency Optimum

The minimum of function (40) is found by taking the zero derivative of (40) according to the magnetic-flux density (41).

$$\frac{\partial P_{net}}{\partial B_{max}} = b_1 f^\alpha B_{max}^{\beta-1} \beta - \frac{2a_1}{f^2 B_{max}^3} = 0 \quad (41)$$

Substituting (36) and (39) into (41) introduces condition (42).

$$P_{cu} = \frac{\beta}{2} P_{fe} \quad (42)$$

#### 2.4.2. Constant Flux Density Optimum

The minimum of function (40) is found by taking the zero derivative of (40), this time according to the frequency (43).

$$\frac{\partial P_{net}}{\partial f} = b_1 f^{\alpha-1} B_{max}^3 \alpha - \frac{2a_1}{f^3 B_{max}^2} = 0 \quad (43)$$

Taking (36) and (39) into (43) introduces condition (44):

$$P_{cu} = \frac{\alpha}{2} P_{fe} \quad (44)$$

#### 2.4.3. Net Losses and Current-Density Setting

Based on the earlier analyses considering the constant frequency, (45) arises.

$$P_{celk} = P_{cu} + P_{fe} = P_{cu} \left( 1 + \frac{2}{\beta} \right) = P_{cu} (1 + \gamma) \quad (45)$$

The  $I^2R$  losses must be led out of the choke by the coil's heat exchange surface,  $S_{conv}$ . Other losses are primarily removed by the surface of the core. The simplest possible model is formed using Newton's law (46).

$$Q = P_{cu} = \rho_{cu} k_u S_w l_{Zavg} J_1^2 = \alpha_k S_{conv} \Delta T \quad (46)$$

Rearranging (46) gives us the required current density (47).

$$J_1 = \sqrt{\frac{\alpha_k S_{conv} \Delta T}{\rho_{cu} k_u S_w l_{Zavg}}} \quad (47)$$

This value gives a fast check of the choke's thermal dimensioning. A more accurate value is obtained by modifying (47) into (48), where  $\Delta T_\alpha$  is the temperature difference between the cooling surface and the ambient, and  $\Delta T_2$  is the temperature difference between the base temperature for the winding-resistance calculation and the average steady-state temperature. The ambient temperature is assumed to be 40 °C.

$$J_1 = \sqrt{\frac{1}{1 + \alpha \Delta T_2} \frac{\alpha_k S_{conv} \Delta T_\alpha}{\rho_{cu} k_u S_w l_{Zavg}}} \quad (48)$$

This formula considers the heat dissipation from the surface of the winding, while it has no information about the temperature of the conductors. The temperature difference

between the insulation and the copper is defined by (49), where  $l_{iz}$  is the insulation thickness and  $\lambda_{iz}$  denotes its thermal conductivity.

$$\Delta T_{\alpha} = \frac{\frac{1}{\alpha_k S_{conv}} \Delta T_1}{\frac{1}{\alpha_k S_{conv}} + \frac{l_{iz}}{\lambda_{iz} S_{conv}}} \quad (49)$$

To calculate the temperature difference, we insert (49) into (48) and obtain (50). The small insulation thickness allows the task to be simplified by treating the outer surface of the winding as a cooling surface.

$$J_1 = \sqrt{\frac{\frac{\alpha_k S_{conv} \frac{1}{\alpha_k S_{conv}} \Delta T_1}{\frac{1}{\alpha_k S_{conv}} + \frac{l_{iz}}{\lambda_{iz} S_{conv}}}}{1 + \alpha \Delta T_2} \frac{1}{\rho_{cu} k_u S_w l_{Zavg}}} = \sqrt{\frac{\frac{\Delta T_1}{\frac{1}{\alpha_k S_{conv}} + \frac{l_{iz}}{\lambda_{iz} S_{conv}}}}{1 + \alpha \Delta T_2} \frac{1}{\rho_{cu} k_u S_w l_{Zavg}}} \quad (50)$$

The heat-transfer coefficient can be considered for natural convection in (50) in two separate calculations. For the vertical walls cooled by the laminar flow, which arises by natural convection, we use (51):

$$\alpha_k = \frac{0.54 \lambda Ra^{0.25}}{L} \quad (51)$$

where  $\lambda$  is the thermal conductivity of air,  $Ra$  is Rayleigh's number, and  $L$  is the height of the wall. Rayleigh's number is defined by (52),

$$Ra = \frac{g \beta \Delta T_{\alpha} L^3}{\nu^2} \frac{c_p \mu}{\lambda} \quad (52)$$

where  $g$  is the gravitation constant,  $\beta$  is the thermal-expansivity coefficient,  $\nu$  is the kinematic viscosity,  $c_p$  represents the specific heat, and  $\mu$  is the dynamic viscosity.

### 3. Design of the Three-Phase Choke

First, the material properties of the winding and the magnetic core must be found. Next, the required inductance and the load characteristics are specified using the operating frequency and the permitted core saturation. We can start by selecting the operative region on the BH curve, which usually lies in the linear zone ending at the knee point.

Assuming a symmetrical three-phase choke with the same parameters of the individual phases, "A", "B", or "C" it is possible to perform an analysis for any phase, such as phase "A", the results of which are also valid for the other phases.

Let us start with the magnetic flux (53).

$$\Psi_A = L_1 I_1 + L_{12} I_2 + L_{13} I_3 \quad (53)$$

As  $L_{12} \cong L_{13} \cong k L_1$ , where  $k \approx -0.5$ , we obtain (54).

$$L_A \approx \frac{3}{2} L_1 \quad (54)$$

While  $L_1$ ,  $L_2$ , and  $L_3$  represent the self-inductances of the individual coils,  $L_{12}$  and  $L_{13}$  form their mutual inductances. Parameter  $k$  is the magnetic-coupling coefficient.

The design process must calculate  $L_1$ , when the targeted application requires the inductance of value  $L_A$ . The parameters  $B_{max}$  and  $J_1$  are optional and define the electromagnetic utilization of the choke. With respect to (54), we state (55).

$$B_{sat} \approx B_{max} \frac{2}{3} \quad (55)$$

The input dimensions are the height of the core  $h_{sl}$ , the gap between the surfaces of two adjacent winding  $d_{win}$ , and the core depth  $a$ .

The preliminary number of turns (not rounded to the integer), are given by (56)

$$N = \frac{L_1 I_1}{B_{sat} S_{fe}} \quad (56)$$

From the current density, the slot-fill factor, the number of turns, and the height of the column of the core, we determine the dimensions of the window for each winding. Based on selected or calculated dimensions, we calculate the average lengths of the flux lines and coil turns and the net  $I^2R$  losses. Next, (12) gives the best equivalent permeability,  $\mu_{opt}$ , which is used in (16) to obtain the first estimate of the air-gap length. Considering three-phase chokes, the air gap must be recalculated to the equivalent length,  $\delta_{net}$ , because the air gaps of the other phases are connected in series-parallel combination with the analyzed phase. Hence, we define (57).

$$\delta_{net} \approx \delta_1 \frac{3}{2} \quad (57)$$

Since we usually find that  $\mu_{opt} > \mu_{eff}$ , few iterations with decreasing  $\delta_1$  may be needed to reach the condition of  $\mu_{opt} \approx \mu_{eff}$ . This algorithm considers the homogenous magnetic flux and, as shown by (18), the fringing flux increases the net inductance. This can be compensated for either by increasing the air gap or by decreasing the number of turns and, hence,  $I^2R$  losses.

Based on (18), the coefficient of the magnetic fringing flux takes the form of (58).

$$k_\sigma = 1 + \frac{2}{a} \delta_1 \quad (58)$$

The final number of turns (59) is then obtained by combining (56) and (58). Here, “nint” refers to “nearest integer”.

$$N' = \text{nint} \left( \sqrt{\frac{\left( \frac{L_1 I_1}{B_{sat} S_{fe}} \right)^2}{1 + \frac{2}{a} \delta_1}} \right) \quad (59)$$

The consequent penalization of the air-gap length (60) offers further improvements in accuracy, moving the proposed analytical approach closer to the FEM solution.

$$\delta'_1 = \delta_1 \left( 1 + \frac{2}{a} \delta_1 \right) \quad (60)$$

The flowchart of the design process is illustrated in Figure 6.

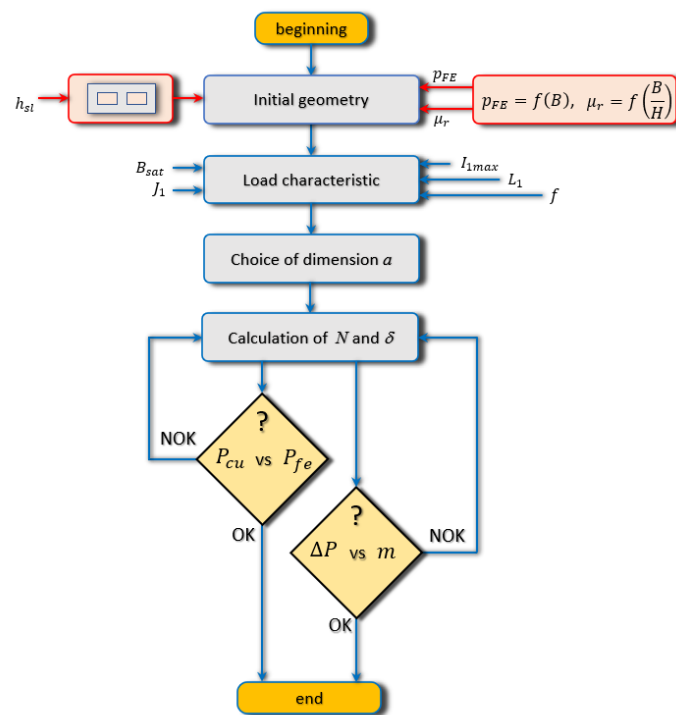


Figure 6. Flowchart of proposed design process.

#### 4. Validation by FEM

The design method was verified by analyzing two geometrical cases (Case “A” and Case “B”), using FEA. The aim of Case “A” was to find the best geometry in terms of total losses and the weight of the design was not considered. On the other hand, Case “B” was to reduce the overall weight, even at the cost of higher losses, but its geometric dimensions were chosen to achieve a significant difference in the number of turns. This case study aims to show that despite the presence of two entirely different geometries, the presented method can design compensation chokes with the same characteristics.

Figure 7 illustrates the quarter symmetry of basic geometrical situation of a magnetic core designed with a square-shaped cross-section.

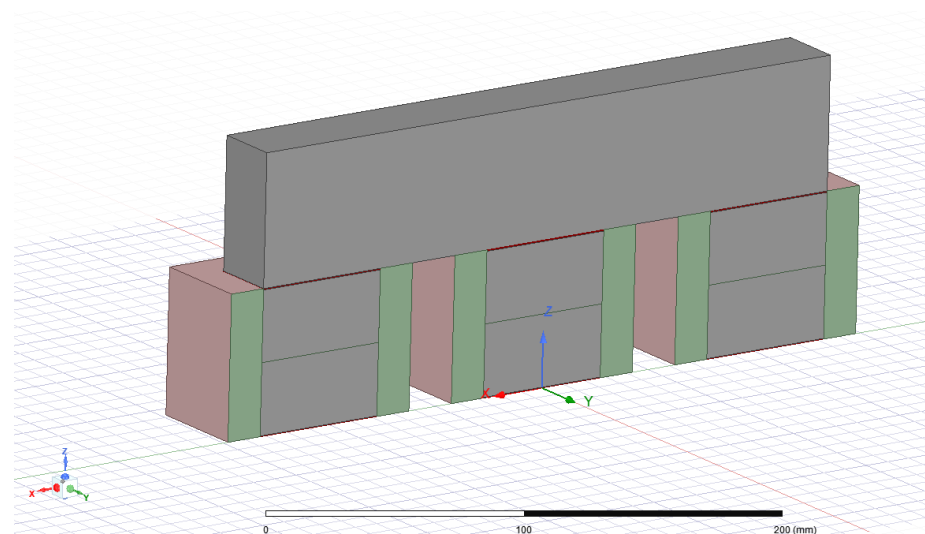


Figure 7. Testing geometry of three-phase compensation choke (quarter symmetry used).

The core was fabricated by Power Core<sup>®</sup>H 075-23L with BH and specific losses curves at 50 Hz, as shown in Figures 8 and 9.

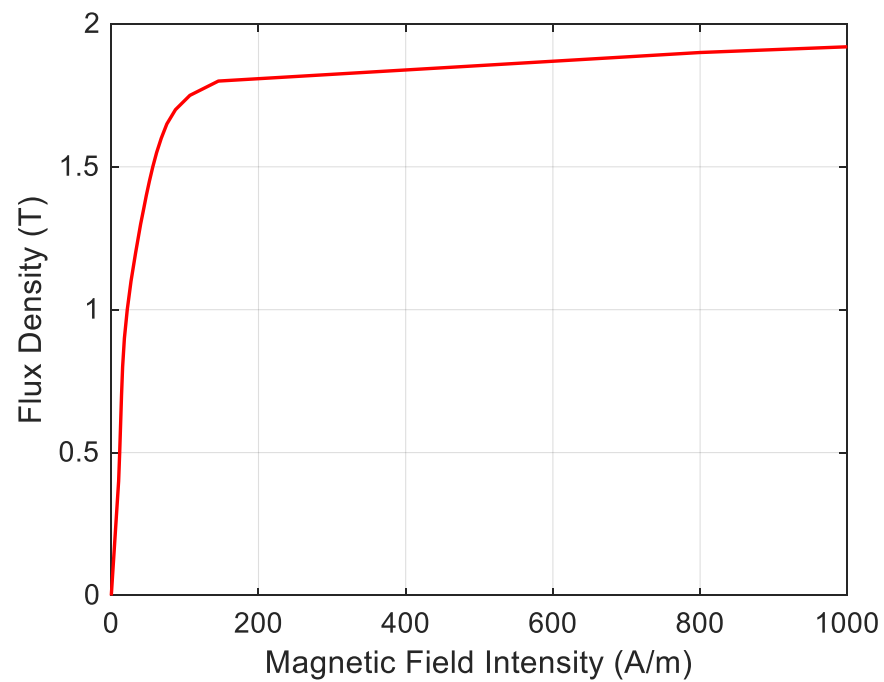


Figure 8. BH curve of material Power Core®H 075-23L.

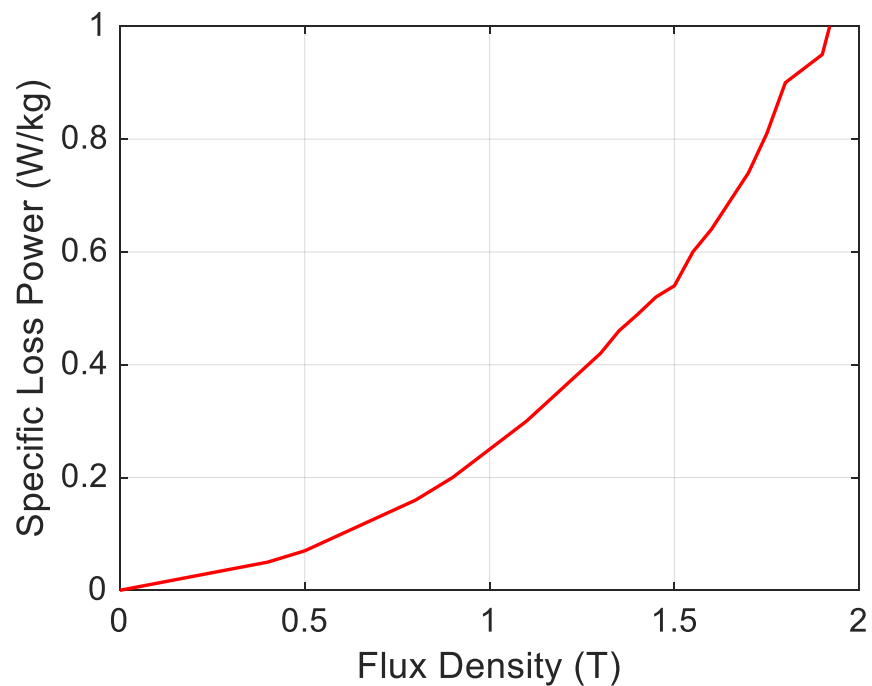


Figure 9. Specific loss power of material Power Core®H 075-23L.

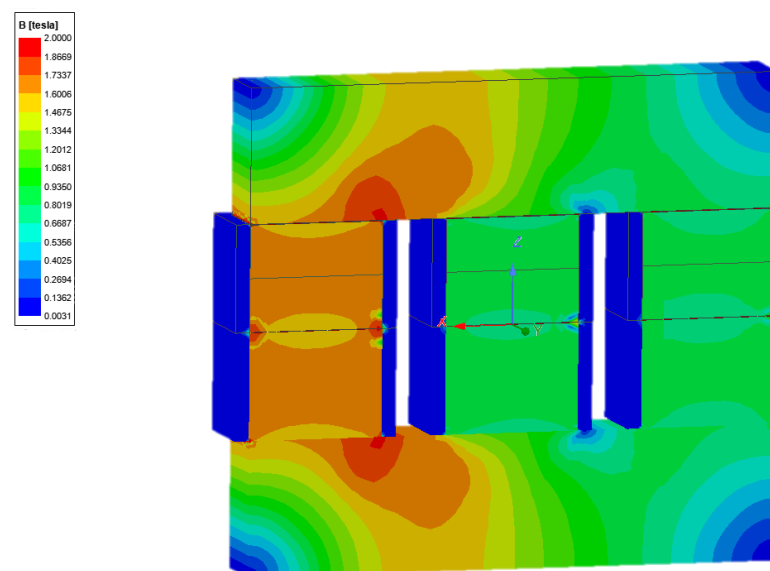
A detailed list of the design parameters obtained by the proposed method can be seen in Table 1. The electromagnetic designs significantly differed in their number of turns, air gaps, weights, and losses, and still provided very similar load characteristics.

**Table 1.** The geometric parameters of analyzed chokes derived from proposed analytical design method.

Case	Case “A”	Case “B”
$I_{rms}$ [A]		7.2
$L_A$ [mH]		103
$f$ [mH]		50
$B_{sat}$ [T]		1.6
$J_1$ [A/mm <sup>2</sup> ]		2.5
$w_{sl}$ [mm]	8.1	15.4
$h_{sl}$ [mm]	120	120
$d_{win}$ [mm]	20	20
$a$ [mm]	75.5	55
$N$ [turns]	114	207
$\delta_1$ [mm]	0.9198	1.707
$\Delta P_{cu}$ [W]	26	41.5
$\Delta P_{fe}$ [W]	23	12
$m_{cu}$ [kg]	4.2	6.7
$m_{fe}$ [W]	43	21.2

#### 4.1. Tested Three-Phase Compensation Choke—Case “A”

The magnetic-flux distribution calculated using FEA is shown in Figure 10. The air-gap-flux density was  $B_1 = 1.64$  T.

**Figure 10.** Magnetic-flux-density distribution in the choke designed for Case “A”.

#### 4.2. Tested Three-Phase Compensation Choke—Case “B”

The magnetic-flux distribution calculated using FEA is shown in Figure 11. The air-gap-flux density was  $B_1 = 1.63$  T.

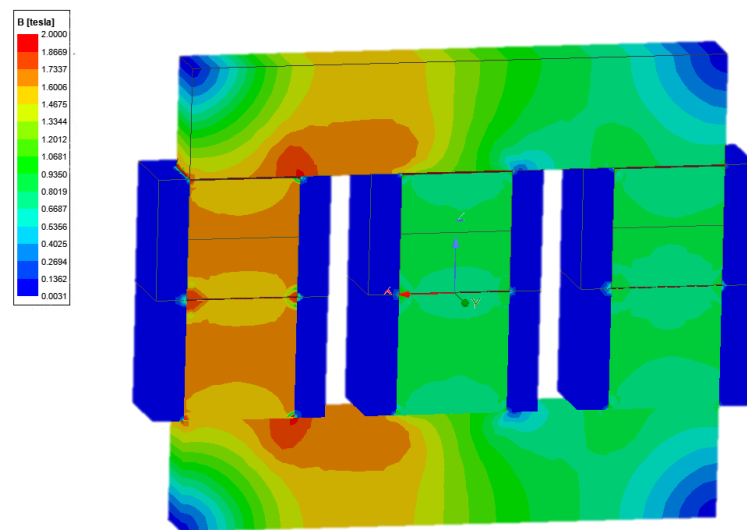


Figure 11. Magnetic-flux-density distribution in the choke designed for Case “B”.

Figure 12 compares the operating characteristics of both chokes. The data were obtained by parametric calculations of the inductances from the FE models shown in Figure 12.

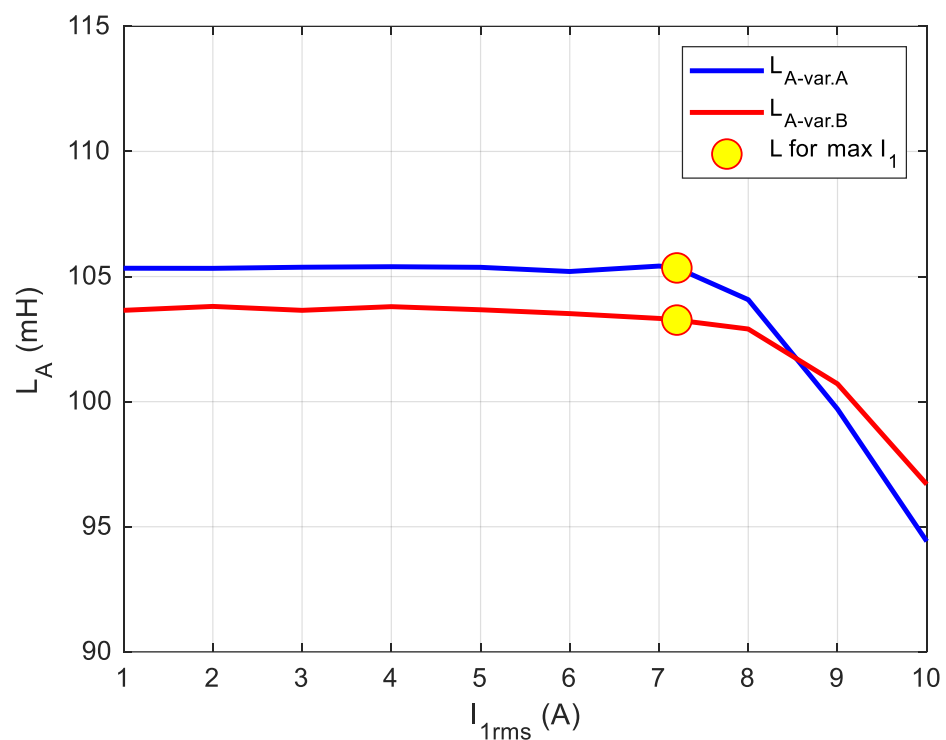


Figure 12. Operational inductances depending on the input current.

Both geometries provide very flat operation characteristics with a constant inductance until reaching the saturation point found at the maximum permitted choke current,  $I_1$ . From the user’s point of view, both chokes are very similar. Minor differences in the inductance values (needing 103 mH) are expected, since the air gap always tunes the final design during the manufacturing process. The results show that the geometry of Case “A” offers approximately 8% lower losses than Case “B”, but its structure is twice as heavy. A compromise between these two cases will always be sought in real applications to meet specific requirements.

## 5. Conclusions

This paper presented a procedure for the first electromagnetic design of a three-phase compensating choke with a flat load characteristic, including advanced analytical-current-density sizing concerning specific temperature conditions.

The proposed method applies to any single- or three-phase choke design including an air gap in the core. It helps find the design with the lowest overall power losses or the with the lightest compensation-choke components.

The method was verified by FEA by comparing the two different choke designs, which were shown to provide very similar operation characteristics, with a constant inductance until reaching the saturation point found at the maximum permitted choke current.

Although the two designs featured entirely different geometric proportions and losses, they were very similar from the user's point of view. The minor differences in inductance values did not constitute a limitation, because the final design is always adjusted by the air-gap tuning during the manufacturing process.

The results show that the geometry of Case "A" has about 8% lower losses than Case "B", but its structure is twice as heavy. In real applications, a compromise between these two cases will always be sought to meet specific requirements.

**Author Contributions:** Conceptualization, methodology and formal analysis by V.K., investigation and data curation L.S., validation and draft preparation M.S. and M.F. All authors have read and agreed to the published version of the manuscript.

**Funding:** This research received no external funding.

**Institutional Review Board Statement:** Not applicable.

**Informed Consent Statement:** Not applicable.

**Data Availability Statement:** Not applicable.

**Acknowledgments:** This research was supported by the Ministry of Education, Youth and Sports of the Czech Republic under the project, OP VVV Electrical Engineering Technologies with High Level of Embedded Intelligence, CZ.02.1.01/0.0/0.0/18\_069/0009855. The authors would also like to thank the Slovak national grant agency, VEGA, for project support (1/0063/21).

**Conflicts of Interest:** The authors declare no conflict of interest.

## References

1. Albulescu, C.T.; Boatca-Barabas, M.-E.; Miclea, S. Greenhouse gas emissions, investment and prices in the EU electricity and gas industry. In Proceedings of the 2019 International Conference on ENERGY and ENVIRONMENT (CIEM), Timisoara, Romania, 17–18 October 2019; pp. 187–190. [CrossRef]
2. Khowja, M.R.; Abebe, R.; Vakil, G.; Walker, A.; Patel, C.; Gerada, C.; Bobba, P.B.; Cascella, G.L. Review on the Traditional and Integrated Passives: State-of-the-Art Design and Technologies. *Energies* **2021**, *15*, 88. [CrossRef]
3. Zhao, J.; Lu, Q.; Yang, D. Experimental and Numerical Analysis of Rotor–Rotor Interaction Characteristics inside a Multistage Transonic Axial Compressor. *Energies* **2022**, *15*, 2627. [CrossRef]
4. Hoffmann, S.; Bock, M.; Hoene, E. A New Filter Concept for High Pulse-Frequency 3-Phase AFE Motor Drives. *Energies* **2021**, *14*, 2814. [CrossRef]
5. Technical Background Document: Accompanying the Report Trends and Projections in Europe 2021. European Environment Agency [Online]. 2021, 25. Available online: <https://www.eea.europa.eu/publications/trends-and-projections-in-europe-2021/technical-background-document/view> (accessed on 14 April 2022).
6. Communication from the Commission to the European Parliament, the Council, the European Economic and Social Committee, and the Committee of the Regions: Investing in a Climate-Neutral Future for the Benefit of Our People [Online]. European Commission, 2020. Available online: <https://eur-lex.europa.eu/legal-content/EN/TXT/?uri=CELEX:52020DC0562> (accessed on 14 April 2022).
7. Subramaniam, U.; Bhaskar, S.M.; Almakhles, J.D.; Padmanaban, S.; Leonowicz, Z. Investigations on EMI Mitigation Techniques: Intent to Reduce Grid-Tied PV Inverter Common Mode Current and Voltage. *Energies* **2019**, *12*, 3395. [CrossRef]
8. Lin, T.-C.; Simachew, B. Intelligent Tuned Hybrid Power Filter with Fuzzy-PI Control. *Energies* **2022**, *15*, 4371. [CrossRef]
9. Lope, I.; Hurley, W.G.; Zhang, J. Common-mode choke design considerations applied to domestic induction heating. In Proceedings of the 2013 48th International Universities' Power Engineering Conference (UPEC), Dublin, Ireland, 2–5 September 2013; pp. 1–5. [CrossRef]

10. Saini, D.K.; Ayachit, A.; Reatti, A.; Kazimierzuk, M.K. Analysis and Design of Choke Inductors for Switched-Mode Power Inverters. *IEEE Trans. Ind. Electron.* **2017**, *65*, 2234–2244. [[CrossRef](#)]
11. Holguín, F.; Prieto, R.; Asensi, R.; Cobos, J. Analytical Winding Power Loss Calculation in Gapped Magnetic Components. *Electronics* **2021**, *10*, 1683. [[CrossRef](#)]
12. Stadler, A.; Huber, R.; Stolzke, T.; Gulden, C. Analytical Calculation of Copper Losses in Litz-Wire Windings of Gapped Inductors. *IEEE Trans. Magn.* **2014**, *50*, 81–84. [[CrossRef](#)]
13. Bachheibl, F.; Gerling, D. Iron loss estimation for highly distorted currents in inverter output chokes. In Proceedings of the 2015 IEEE International Electric Machines & Drives Conference (IEMDC), Coeur d’Alene, ID, USA, 10–13 May 2015; pp. 1260–1264. [[CrossRef](#)]
14. Liu, Y.; See, K.Y.; Simanjorang, R. 3-D modeling of common mode choke for thermal analysis. In Proceedings of the 2017 Asia-Pacific International Symposium on Electromagnetic Compatibility (APEMC), Seoul, Korea, 20–23 June 2017; pp. 79–81. [[CrossRef](#)]
15. Valchev, V.C.; Todorova, T.P.; Yankov, P.V.; Bossche, A.V.D. Design considerations and loss analysis of DC chokes. In Proceedings of the 19th International Symposium on Electrical Apparatus and Technologies (SIELA), Bourgas, Bulgaria, 29 May–1 June 2016; pp. 1–3. [[CrossRef](#)]
16. Hussain, I.; Woo, D.-K. Self-Inductance Calculation of the Archimedean Spiral Coil. *Energies* **2021**, *15*, 253. [[CrossRef](#)]
17. Park, J.-M.; Byun, H.-J.; Kim, B.-J.; Kim, S.-H.; Won, C.-Y. Analysis and Design of Coupled Inductor for Interleaved Buck-Type Voltage Balancer in Bipolar DC Microgrid. *Energies* **2020**, *13*, 2775. [[CrossRef](#)]
18. Duppalli, V.S.; Sudhoff, S. Power density comparison of three-phase AC inductor architectures. In Proceedings of the 2017 IEEE Electric Ship Technologies Symposium (ESTS), West Lafayette, IN, USA, 14–17 August 2017; pp. 217–224. [[CrossRef](#)]
19. Heldwein, M.L.; Dalessandro, L.; Kolar, J.W. The Three-Phase Common-Mode Inductor: Modeling and Design Issues. *IEEE Trans. Ind. Electron.* **2010**, *58*, 3264–3274. [[CrossRef](#)]
20. Hilal, A.; Cougo, B. Optimal inductor design and material selection for high power density inverters used in aircraft applications. In Proceedings of the 2016 International Conference on Electrical Systems for Aircraft, Railway, Ship Propulsion and Road Vehicles & International Transportation Electrification Conference (ESARS-ITEC), Toulouse, France, 2–4 November 2016; pp. 1–6. [[CrossRef](#)]
21. Liao, H.; Chen, J. Design process of high-frequency inductor with multiple air-gaps in the dimensional limitation. *J. Eng.* **2021**, *2022*, 16–33. [[CrossRef](#)]
22. Zhang, X.; Xiao, F.; Wang, R.; Kang, W.; Yang, B. Modeling and Design of High-Power Enhanced Leakage-Inductance-Integrated Medium-Frequency Transformers for DAB Converters. *Energies* **2022**, *15*, 1361. [[CrossRef](#)]
23. Available online: <https://product.tdk.com/en/products/magnet/technote/designguide.html> (accessed on 3 October 2022).